Research Article | Vol. 32, No. 13 / 17 Jun 2024 / Optics Express 22110
Optics EXPRESS

Surface roughness and wave slope statistics from the multi-spectral polarimetric imaging of the ocean surface

MATEUSZ MALINOWSKI,[1] ALEXANDER GILERSON,[1,2,*] EDER HERRERA-ESTRELLA,[1,2] ROBERT FOSTER,[3] JACOPO AGAGLIATE,[1] AND MICHAEL ONDRUSEK[4]

[1]The City College of New York, 160 Convent Ave., New York, NY 10031, USA
[2]Earth and Environmental Sciences, The Graduate Center, New York, NY 10031, USA
[3]Remote Sensing Division, Naval Research Laboratory, Washington, DC 20375, USA
[4]NOAA/NESDIS/STAR, College Park, MD 20740, USA
[*]gilerson@ccny.cuny.edu

Abstract: The polarization of light in Ocean Color (OC) applications provides important information about atmospheric parameters, water composition, and the ocean surface. The Stokes vector components and the degree of linear polarization of light contain useful information about the air-water interface, including ocean surface roughness. We present polarimetric measurements and analysis of the ocean wave slopes at several bands. Data is acquired with a Teledyne DALSA camera, which uses a polarizer-on-chip focal plane of 1232×1028 super-pixels, where each pixel is made of four subpixels with 0-, 90-, 45- and 135-degrees orientation of polarization. We present a modified version of the Polarization Slope Sensing (PSS) technique [Zappa et al., 2008] for the non-contact detection of wave slopes and demonstrate a good performance of the updated algorithm in several conditions where the original technique was not applicable. Derived wave slopes are presented for various aquatic and atmospheric environments, including during VIIRS Cal/Val cruises and at a near-shore pier. The results are shown to be consistent with theoretical wave slope models.

1. Introduction

An ocean surface slope distribution and relationships between slope variances and wind speed first established by Cox and Munk [1], further CM, almost sixty years ago are still widely used today in OC applications [2,3] as well as in the remote estimation of surface wind speeds [4,5], sea surface temperature [6], and in aerosols and clouds retrievals [7]. The CM model was successfully validated by the analysis of observations from the Polarization and Directionality of the Earth's Reflectances (POLDER) satellite sensor [8], from the spectral photometer on the coastal platform at the mouth of the Chesapeake Bay [9], and from laser reflections [10–14] measurements that were carried out in the visible part of the spectrum and IR [15]. In most cases, the CM model was confirmed with higher uncertainties in the field measurements than those predicted by the CM model.

In OC applications, the wind-roughened ocean surface plays a role in the calculation of the transmission of sunlight and diffuse skylight from the top of the atmosphere into the water and then back to the satellite sensor [16,17]. Uncertainties in remote sensing reflectance) estimations are based on the state of the wind-roughened ocean surface and the elimination of the sky component reflected from the surface [2,18,19]. For satellite applications, such effects are included in the atmospheric correction algorithm [2,3]; for ship-borne measurements, the reflectance coefficient of the skylight from the sea surface is pre-calculated for viewing geometries recommended for such observations [2,20]. Because of the importance of the CM model to OC

#521650 https://doi.org/10.1364/OE.521650
Journal © 2024 Received 14 Feb 2024; revised 17 May 2024; accepted 22 May 2024; published 3 Jun 2024

Optics EXPRESS

estimations, the model's applicability in various conditions, especially in coastal waters, requires additional validation.

Polarized light measurements can be associated with commonly measured spectral signatures to provide additional important information in multiple applications, including the parametrization of atmospheric aerosols [21–23] ocean particulates [24–29], and ocean surfaces [30,31]. As such, the utilization of polarimetric measurements has been viewed as the next step in improving OC applications [32]. The polarization component is critical for the accurate determination of the reflectance coefficient from the sea surface (ρ), which is widely used in the processing of above water measurements and atmospheric correction models [2,20,33]. A combination of multi-angular and hyperspectral polarimetric data can take advantage of the strong sensitivity of polarization signals to the illumination and viewing geometry as well as the microphysics of in-water particulates [32]. NASA's Plankton, Aerosol, Cloud, and ocean Ecosystem (PACE) mission [34], currently in its final development phase, in addition to the hyperspectral Ocean Color Instrument (OCI), will have two polarimeters on board with different spectral and angular capabilities. Some results from polarimetric imaging of the ocean surface were recently presented for several water types, wind conditions, and multiple illumination and viewing conditions, and combined with the analysis of the related uncertainties [35]. Retrievals of attenuation to absorption ratios were also recently considered as an application for polarimetric data [36].

A polarization-based technique called Polarization Slope Sensing (PSS) was proposed to determine wave slopes without direct contact of the sensor with the ocean surface [37] and was further applied to measurements of wave slope statistics at different wave regimes [38]. A special polarimeter was developed for the application of this technique [39]. The technique was recommended for measurements in cloudy sky conditions to minimize polarization of the sky. This limits its applicability, especially in OC cruises, where sunny conditions are required to compare in-situ and satellite data. Recently, we proposed a modified polarization technique [40,41], which provided more reliable wave slope estimations. In this work, from multiple ocean cruises, we present results of measurements of Stokes vector components at several spectral bands carried out in imaging mode using a novel polarization camera and of wave slopes retrievals made using a further modified Polarimetric Slope Sensing technique (abbreviated as PSSm), for which applicability constraints are less strict. Wave slope variances are compared with Cox-Munk relationships. The sensitivity of variance measurements to the wavelength is also discussed.

2. Methods

2.1. Instrumentation and data processing

Measurements were carried out with a unique City College of New York (CCNY) imaging system for multi- and hyperspectral polarimetric above water observations, shown in Fig. 1. The system consists of a snapshot hyperspectral imaging spectrometer (Cubert, Germany) with no moving parts and a polarimetric imaging camera (Genie Nano Series, Teledyne DALSA, Teledyne Technologies Inc., USA). Only results from the camera will be discussed. The camera is based on the Sony IMX250MZR image sensor with 2464 (H) $\times$ 2056 (V) pixels, where each 2×2 - pixel area consists of four subpixels that are equipped with polarizers oriented at 0°, 90°, 45° and -45°, respectively. This sensor was integrated into the Teledyne DALSA M2450 camera and calibrated using a handheld GER spectroradiometer and a Lambertian plate. The camera is designed for operation in panchromatic mode between 400-950 nm. However, in our implementation, it was combined with a filter wheel (Finger Lakes Instrumentation, NY) containing five color band-pass filters (AVR Optics, NY) with rectangular transmission spectra at the following center wavelengths (bandwidths) 442 (42), 494 (41), 550 (32), 655(40) and 684(24) nm. The camera with the filter wheel was assembled on top of the imager and a lens in front of the camera provides a rectangular field of view (FOV) (HFOV x VFOV = 29.2° x 38.4°). Typical integration time was 20 milliseconds (ms) for water measurements, 5 ms for sky

Optics EXPRESS

measurements, and 0.5 ms for Lambertian reflectance plaque measurements. Videos of the water surface were acquired with a typical frame rate of about 10 frames/second- and 8-bit digitization. The user interface provided by the manufacturer was integrated with the filter wheel interface to allow for the automatic acquisition of videos and images of polarization components. These images and videos are then reprocessed to get images and videos of Stokes vector components, the degree of linear polarization (DoLP), and the angle of linear polarization (AoLP). The system was deployed during several recent Visible-Infrared Imaging Radiometer Suite (VIIRS) Ocean Color Cal/Val Cruises and near shore in Brooklyn, NY.

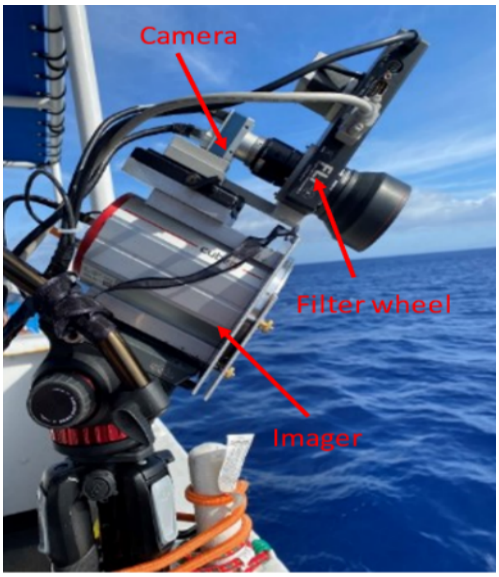

Fig. 1. Hyper- and multi-spectral polarimetric imaging system (Genie Nano Series polarization camera is on top).

Data was recorded in sets of videos of 100 frames and each filter measurement was taken sequentially starting from 442 nm to 684 nm. There is about a minute time difference between each filter measurement, so the sea-air interface interactions can change significantly between the first 442 nm filter and the 684 nm filter measurements. The details of data processing are elaborated below in the analysis of characteristics of wave slopes and wave spectra.

2.2. Camera calibration

The polarization camera was calibrated using a handheld GER-1500 spectroradiometer (Spectra Vista Corp., USA) and a Spectralon white plate with Lambertian properties. The radiance of the skylight reflected from the white plate and recorded by the spectroradiometer is unpolarized. The system was tested to show linear response with exposure time, while the dark current of the system was small and considered negligible. To convert 8-bit digitization to radiance values a 3-D calibration coefficient K (x and y pixel coordinates and wavelength λ) was used for the five corresponding color filters. In Eq. (1) the recorded GER-1500 spectroradiometer radiance ($I_G(\lambda)$) for the light reflected from the plate is multiplied by the exposure time of the camera measurement over the 8-bit digitization pixel value $P_c(x, y, \lambda)$ from the camera after subtracting the dark current $D_c(x, y, \lambda)$. Muller matrix $\boldsymbol{M_{system}}$ [3,3] is used to correct any inherent polarization introduced by the system as shown in Eq. (2), however, with unpolarized light, the elements of the matrix in

Optics EXPRESS

the two right columns cannot be determined.

$$K(x, y, \lambda) = \frac{I_G(\lambda) \cdot exposure\_time(\lambda)}{P_c(x, y, \lambda) - D_c(x, y, \lambda)} \tag{1}$$

$$\begin{bmatrix} I_c^0 \\ Q_c^0 \\ U_c^0 \end{bmatrix} = \frac{1}{K} \begin{bmatrix} M_{11} & M_{12} & M_{13} \\ M_{21} & M_{22} & M_{23} \\ M_{31} & M_{32} & M_{33} \end{bmatrix} \begin{bmatrix} I_G \\ 0 \\ 0 \end{bmatrix} \tag{2}$$

On the left side of Eq. (2) is the Stokes vector measured by the camera with unpolarized light at the input. Additional calibration measurements with and without the polarizer at two different orientations (0°, 45°) in front of the camera were required following the approach of Gordon et al. [42]. Thus, each Stokes vector measured at the pixel was used to determine other elements of the Mueller matrix as shown in Eq. (3a) in general formulation, which becomes Eq. (3b) when using 0° orientation polarizer. The same procedure was carried out for the polarizer with 45° orientation.

$$\boldsymbol{S_c} = \frac{1}{K} \cdot \boldsymbol{M_{system}} \cdot \boldsymbol{M_{polarizer}} \cdot \boldsymbol{S_{incident}} \tag{3a}$$

$$\begin{bmatrix} I_c^H \\ Q_c^H \\ U_c^H \end{bmatrix} = \frac{1}{K} \begin{bmatrix} M_{11} & M_{12} & M_{13} \\ M_{21} & M_{22} & M_{23} \\ M_{31} & M_{32} & M_{33} \end{bmatrix} \cdot 0.5T \begin{bmatrix} 1 & 1 & 0 \\ 1 & 1 & 0 \\ 0 & 0 & 0 \end{bmatrix} \begin{bmatrix} I_G \\ 0 \\ 0 \end{bmatrix} \tag{3b}$$

where T is the unpolarized transmittance of the polarizer.

Thus, the Stokes vector of light from the object $[I, Q, U]^{\mathrm{T}}$ (the above water or sky radiance) measured by the camera was modified by the system to the Stokes vector $[I_c^m, Q_c^m, U_c^m]$ as shown in Eq. (4) and was determined from the measured Stokes vector according to Eq. (5).

$$\begin{bmatrix} I_c^m \\ Q_c^m \\ U_c^m \end{bmatrix} = \frac{1}{K} \begin{bmatrix} M_{11} & M_{12} & M_{13} \\ M_{21} & M_{22} & M_{23} \\ M_{31} & M_{32} & M_{33} \end{bmatrix} \begin{bmatrix} I \\ Q \\ U \end{bmatrix} \tag{4}$$

$$\begin{bmatrix} I \\ Q \\ U \end{bmatrix} = K\, M^{-1} \begin{bmatrix} I_c^m \\ Q_c^m \\ U_c^m \end{bmatrix} \tag{5}$$

2.3. Areas of study

Above-water shipborne observations were carried out during the National Oceanic and Atmospheric Administration (NOAA) VIIRS Cal/Val cruise, which took place between the 20th and 29th of April 2021 in the Northern Gulf of Mexico, originating from Pascagoula, MS (Fig. 2). Data was collected at several stations including a few stations in the vicinity of the WaveCIS Aerosol Robotic Network for Ocean Color (AERONET-OC) site. Water conditions varied from clear, open ocean type waters to coastal waters closer to the shore. Another VIIRS Cal/Val cruise took place in Hawaii from the 9th to the 17th of March 2022 southeast of the island of Oahu around the new and old Marine Optical Buoy (MOBY) sites. The third cruise was from March 2nd to the 11th in 2023 on the West Coast near Newport, OR. Measurements were also carried out from the Steeplechase Pier in Coney Island, Brooklyn, NY. The height of the imaging system

Optics EXPRESS

on the ships and on the platform was about 10 meters. During ocean cruises and at the pier, the imaging system was installed on a vertical pole connected to the railing on the deck of the ships with the optical axis oriented at 40° from the nadir for the observations of the water surface and at 40° from the zenith for sky observations. The relative solar azimuth angle was usually fixed at $\varphi_v = 90°$ with some variations during cruise measurements due to small ship movements. The FOV of the polarization camera covered the range of viewing angles from 25° to 55° with respect to nadir (water-viewing) and zenith (sky-viewing).

Fig. 2. Geographical Locations of VIIRS CAL/VAL Cruise stations for a) 2022 Hawaii, b) 2021 Gulf of Mexico, c) 2023 Northwest Coast of US, and d) Brooklyn Pier.

In each full measurement cycle, water and sky observations were complemented by measurements of the downwelling irradiance using a Spectralon white plate, and measurements of the dark noise. At the same time, spectral data from the water, sky, and the plate were acquired by a GER-1500 spectroradiometer (Spectra Vista Corp., USA); aerosol optical thickness (AOT) was measured by a Microtops II Sun-photometer at wavelengths 380, 500, 675, 870 and 1020 nm (Solar Light Company LLC, USA). Wind speed WS was measured by the ship instrumentation in ocean cruises and by a handheld anemometer at the pier.

3. Results

3.1. Polarimetric imaging, comparison of field measurements

Polarization components measured by the camera $I^m_{c0,}$ I^m_{c45}, I^m_{c90}, I^m_{c135} were used to calculate Stokes vector (**S**) components for each pixel by Eq. (6).

$$I^m_c = (I^m_{c0} + I^m_{c45} + I^m_{c90} + I^m_{c135})/2 \tag{6a}$$

$$Q^m_c = I^m_{c0} - I^m_{c90} \tag{6b}$$

$$U^m_c = I^m_{c45} - I^m_{c135} \tag{6c}$$

which were converted into the vector $[I, Q, U]^{\mathrm{T}}$ following Eq. (5). Using these components, the DoLP and AoLP can be calculated by Eq. (7) and (8) for each pixel. The DoLP and AoLP are

Optics EXPRESS

used in the PSS algorithm to calculate the wave slopes.

$$DoLP = \sqrt{(Q^2 + U^2)/I^2} \tag{7}$$

$$AoLP = 1/2\tan^{-1}(U/Q) \tag{8}$$

Spectra of I, Q/I, U/I components and DoLP from station 6 of the Hawaiian cruise are shown in Fig. 3. These spectra are the result of averaging over 100 frames recorded for each color filter before being processed into the Stokes components and DoLP for five different viewing angles VA (25°, 30°, 40°, 50°, 55°). Each of the VA regions of the camera consists of 100×100 pixels in the center, totaling 10000 pixels for each viewing angle; for 100 frames it gives a total of a million data points. For open ocean water measurements, the DoLP increases with wavelength, which is due to the low concentrations of colored dissolved organic matter (CDOM) and chlorophyll-rich particles and corresponding low absorption in the blue part of the spectra. Higher absorption reduces the number of scattering events and increases the DoLP [43]. Thus, the DoLP spectra for open ocean waters resemble the absorption spectrum of pure water. Stokes vector components spectra for coastal waters at station 1 off the port of Pascagoula, MS in the Gulf of Mexico are shown in Fig. 4. In this case in CDOM – rich waters with high absorption in the blue, the DoLP is high in the blue and red part of the spectrum. I component spectra in Figs. 3 and 4 at 40° are very close to the GER spectra, which confirms the good quality of camera measurements and calibration.

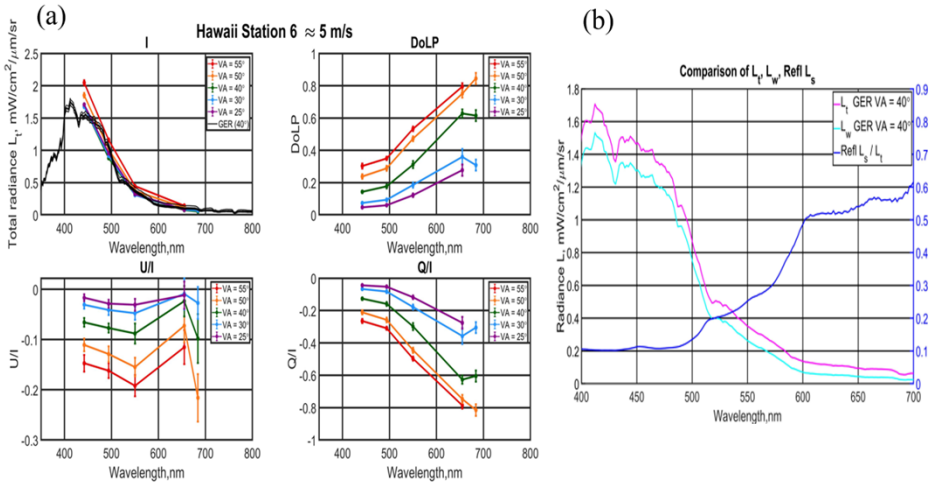

Fig. 3. a) Hawaii Station 6 Stokes vector components spectra and DoLP (open ocean 03/11/22, UTC-23:16, solar zenith angle 29.1°) and b) corresponding L_t, L_w, reflectedL_s/L_t from the GER.

In Figs. 3 and 4 on the right GER spectra of L_t are shown together with the spectra of the water leaving radiance L_w estimated by the subtraction of the sky-reflected component L_s from L_t, showing that the contribution of the L_s is small in both cases and that the spectra of the Stokes vector components and DoLP are mostly defined by the spectra of L_w, while the reflected skylight contribution L_s is of interest in the PSS technique. In the same figures, the ratio of the reflected skylight to the total radiance L_s/L_t is shown demonstrating the maximal sky contribution in red in the Hawaii station and in blue in the GoM station.

Fig. 5 shows the images of I, Q/I, U/I, and the DoLP obtained at the same stations: station 6 of Hawaii at moderate wind speed and the Gulf of Mexico station 1 at low wind speed for the 550 nm, demonstrating the spatial distribution of the Stokes components and the DoLP in the FOV. Photos of the water color and sky conditions are shown at the bottom.

Optics EXPRESS

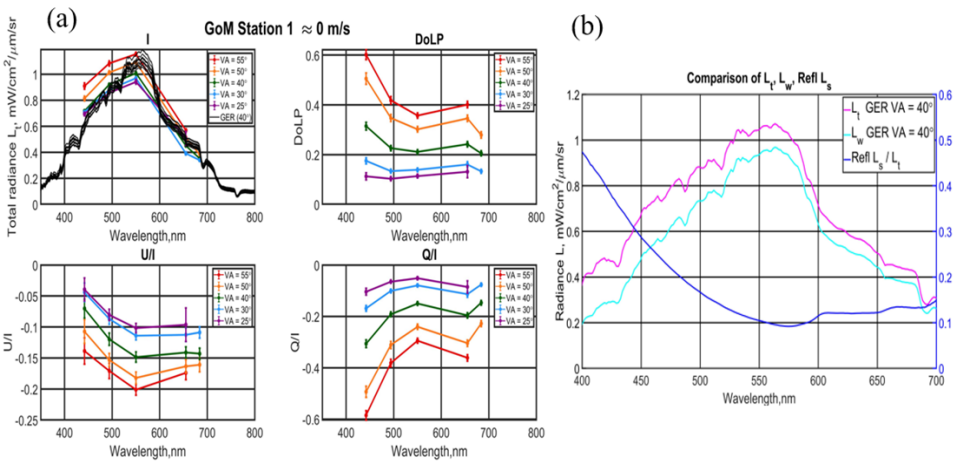

Fig. 4. a) GoM station 1 Stokes vector components spectra and DoLP (coastal waters 04/20/21, UTC-20:30, solar zenith angle 52°) and b) corresponding L_t, L_w, reflected L_s/L_t from the GER.

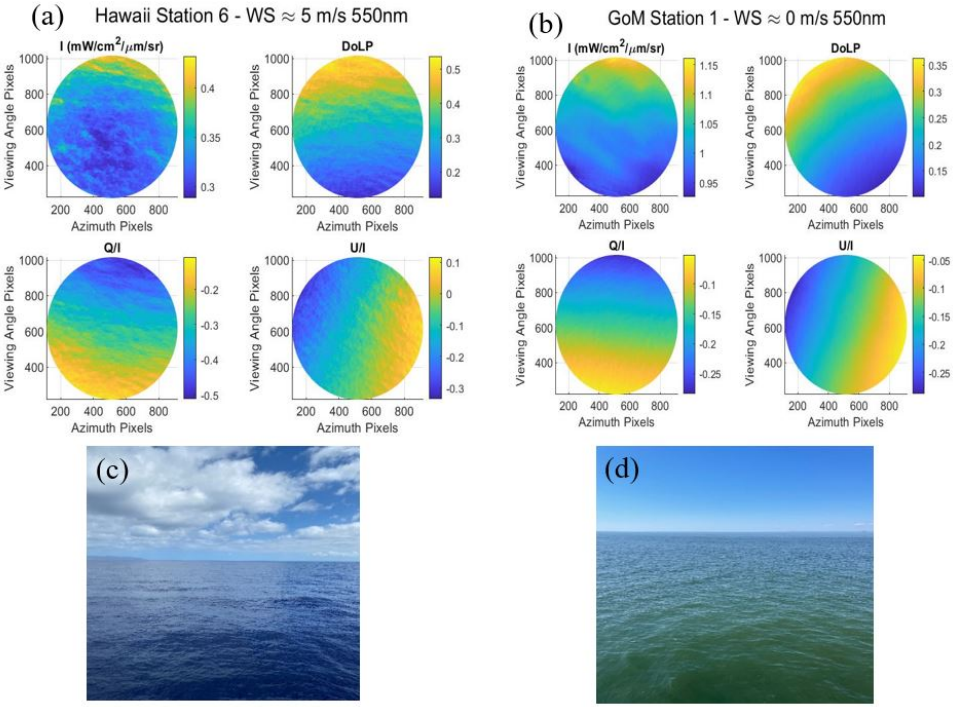

Fig. 5. Comparison of Stokes components and DoLP in the FOV for a) Hawaii station 1 and b) Gulf of Mexico Station 1 at 550 nm, c) and d) photos of the water color and sky conditions at the stations.

Optics EXPRESS

3.2. Polarimetric slope sensing technique and Cox and Munk statistics

The Polarimetric Slope Sensing (PSS) technique [37] was suggested to retrieve the bi-directional slope of a given wave facet imaged by the polarization camera. The slope in this case is defined by a pair (θ, φ) of angles, as shown in Fig. (6(a)) similar to Fig. 1 in [37], respectively identifying the angle between the incident sky light and the normal of the facet θ together with the deviation angle $\Delta\theta$ and the angle between the line of the intersection of the reflection and image planes and the horizontal line φ. The method, in its original implementation, takes advantage of the reflection Mueller matrix, which is a function of the Fresnel reflection coefficients that are, in turn, the function of the incidence and transmission angles. These are ultimately tied together by the known refractive index of water and Snell's law. The angle $\Delta\theta_0$ is determined from the deviations of the DoLP ($\Delta DoLP_0$) in the Fig. (6(b)) DoLP vs VA curve as the difference between the measured DoLP at the specific VA and the DoLP at the same VA under the assumption that the wave slopes have zero mean. The angle φ is defined as $\varphi = \text{AoLP} + 90°$. This technique was expected to work in idealized conditions of a non-polarized sky and in the absence of upwelling polarized light from the water. Even in cloudy sky conditions, as originally suggested, such requirements are difficult to satisfy in full.

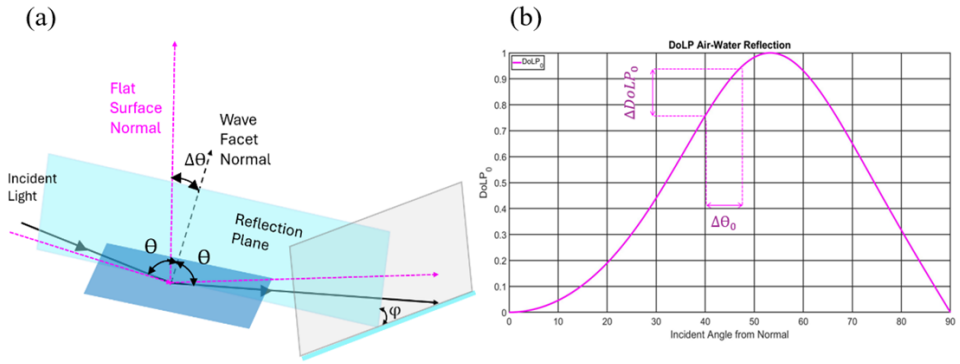

Fig. 6. a) The geometry of slope observations: incident angle θ, deviation angle Δθ and polarization orientation φ; b) Degree of polarization $DoLP_0$ based on Fresnel equations, example of estimated $\Delta\theta_0$ from the $DoLP_0$ curve.

The DoLP vs VA curve in Fig. (6(b)) is expected to be, in the first approximation, independent of the wavelength. However, OC measurements usually require clear skies and therefore contain polarized light from the sky and the water. As was shown in Fig. 3 and 4, the spectrum of measured above water DoLP is significantly affected by the DoLP of the water leaving radiance. This effect is smaller in cloudy conditions, but it still exists. Referring to Fig. (6(b)), which represents ideal conditions described in [37], the VA is 40°, and the DoLP produced from a flat surface with a slope of zero would be about 0.75. In this case, the observed DoLP is about 0.92, ($\Delta DoLP_0 \approx 0.17$), which corresponds to an incident angle of 47^0, and therefore a facet slope of $\Delta\theta_0 \approx 7^0$.

In our modified Polarimetric Slope Sensing technique called PSSm improvements included: a) estimation of the ΔDoLP not from the ideal curve in Fig. (6(b)) but from the actually measured DoLP vs VA curve of the scene; b) selection of a spectral band used for such measurements by taking an advantage of the measurements by the camera with different color filters, and c) elimination of the impact of the water leaving radiance L_w on the $\Delta DoLP$ to ensure that $\Delta\theta$ is determined only from the reflected sky radiance and thus directly related to the wave facet orientation. So, we used the actual DoLP curves measured at the scene instead of the ideal curve represented by the Fresnel equations (Fig. 6(b)). In our version, the instantaneous slope deviation

Optics EXPRESS

angle $\Delta\theta_1$ (which still includes the impact of L_w) from each pixel is based on $\Delta DoLP$ from the DoLP vs VA curve directly measured by the camera (averaged over 100×100 pixels and all recorded frames), not from the $\Delta DoLP_0$ illustrated in Fig. 6(b) (the ideal Fresnel curve). The slope angle $\Delta\theta_2$, which is ultimately used for estimation of the wave facet slope is determined after the elimination of the L_w contributions to the DoLP. Examples are shown in Fig. 7 for Hawaii and GOM stations with angles annotated on the GOM station graph. 443 nm curve was used in the processing for GoM and the 655 nm curve for the Hawaii cruise.

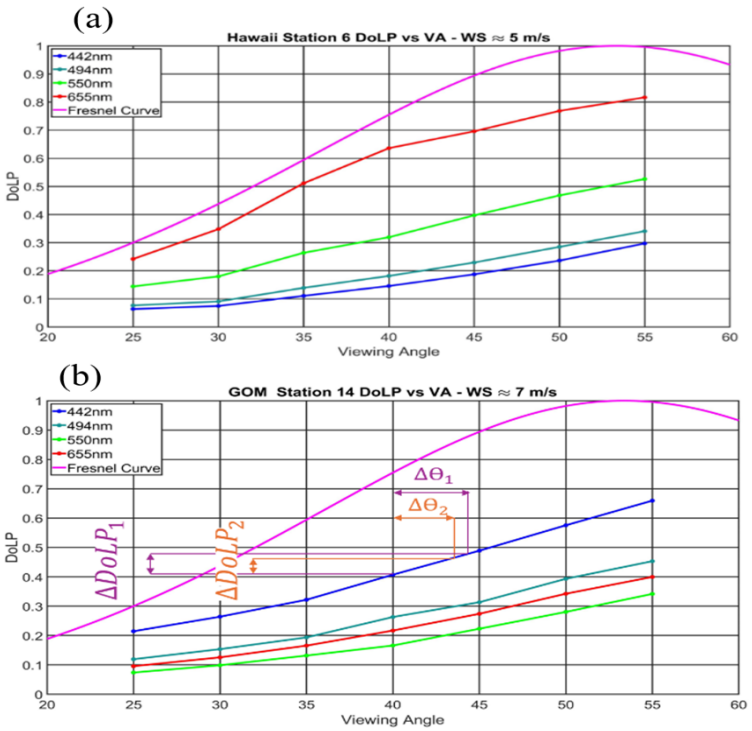

Fig. 7. Theoretical and measured DoLP curves for a) Hawaii and b) GOM stations.

The measured DoLP curves in Fig. 7 include the contributions from the sky and water polarization. Camera measurements allow simultaneous analysis of such relationships at several viewing angles in the FOV, and several wavelengths in a sequence using different color filters. While slope characteristics should not depend on either viewing angle or wavelength, VA = 40° was selected for the analysis as the reflected light has minimal impact from the sun glint at the azimuth angle of 90° used in observations [35].

Separate measurements of the sky by the camera were often not included in the field datasets for logistical reasons, and the Stokes vector of the sky was estimated from the vector radiative transfer simulations (VRT). Such simulations using RayXP code [44] showed that the Stokes vector of the skylight S_{sky} at the sky viewing angle in the range of 30-50° and azimuth angle 90° (conditions typically used in measurements) remains approximately the same for the specific wavelength. The Stokes vector of the sky reflected from the water surface was determined for the viewing angle and wind speed through the multiplication by the Mueller matrix $\boldsymbol{M}_{surf}$ calculated for these conditions using Monte-Carlo simulations [45] at 443 nm with the assumption that the matrix is independent of the wavelength. For low aerosol optical thicknesses well below 0.5, which were observed in the field experiments, $\boldsymbol{M}_{surf}$ components vary in a small range as a function of the wind speed WS [45], they only slightly differ from those calculated by Fresnel

Optics EXPRESS

equations for the WS = 0 and the differences did not have any substantial effect on wave slope retrievals. So, the Stokes vector of the skylight reflected from the water surface.

$$\boldsymbol{S_{refl}} = \boldsymbol{M_{surf}}\boldsymbol{S_{sky}} \tag{9}$$

$\boldsymbol{S_{refl}}$ was subtracted from the measured vector **S** to determine components of the Stokes vector of the water leaving radiance:

$$\boldsymbol{S_w} = \boldsymbol{S} - \boldsymbol{S_{refl}} \tag{10}$$

Components of $\boldsymbol{S_w}$ and $\boldsymbol{S_{refl}}$ for the GoM station as a function of the viewing angle for four filters is shown in Fig. 8. ($\mathbf{S_w}$ components are shown only for the comparison with $\boldsymbol{S_{refl}}$ and were not used in the retrieval algorithm). Deviation angles $\Delta\theta_1$ for each filter determined from the average DoLP curves (Fig. 7) were then applied to the reflected sky curves from the corresponding filter (Fig. 8) as deviations from 40° to determine deviations of ΔQ_{refl} and ΔU_{refl} due to the reflected sky only. Taking into account that ΔU_{refl} is much smaller than ΔQ_{refl}

$$\Delta DoLP_2 = \sqrt{\Delta Q_{refl}^2 + \Delta U_{refl}^2}/\ I \ \approx \Delta Q_{refl}/I \tag{11}$$

where I is the total radiance (reflected sky + water-leaving) directly measured by the camera. This $\Delta DoLP_2$, which does not have a contribution by the water-leaving polarization, is used to determine the true deviation angle $\Delta\theta_2$ from the average DoLP curves (Fig. 7). The total radiance I (not I_{refl}) is used in Eq. (11) because $\Delta DoLP_2$ is then applied to the DoLP curve to determine $\Delta\theta_2$ in Fig. 7; this curve contains both water-leaving and reflected sky contributions and it is important that only sky contribution determines $\Delta\theta_2$. Examples of $\Delta DoLP$ and $\Delta DoLP_2$, which correspond to the deviations $\Delta\theta_1$ and $\Delta\theta_2$, respectively, are shown in Fig. 7. Rotation matrices in the calculation of the Stokes components were not applied since this process would require knowledge of the wave slopes, which we are trying to determine. This is not supposed to affect most of the results since the determined wave slopes are averaged over a large number of observations (pixels and frames). However, it may affect the quality of data presented below in Fig. 10, where instantaneous slopes are shown for each pixel.

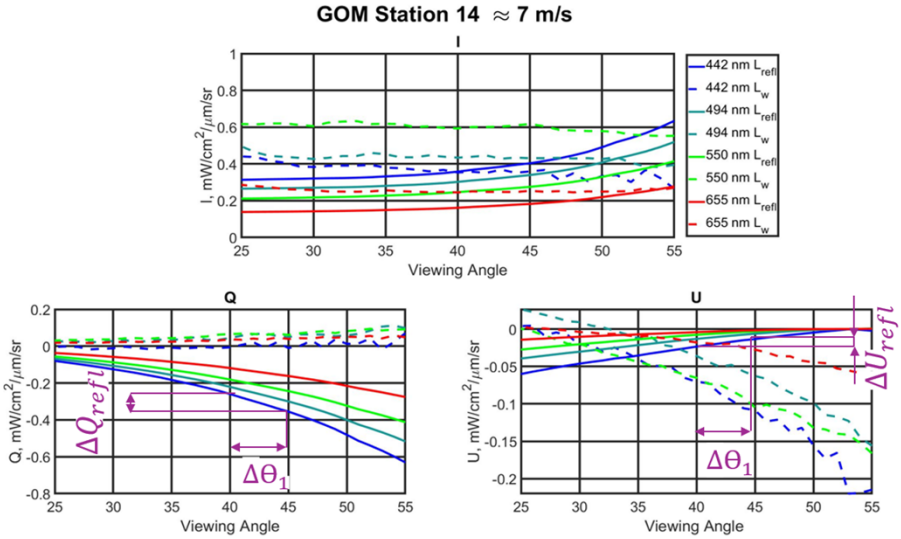

Fig. 8. *I*, *Q* and *U* components of Stokes vectors $\boldsymbol{S_{refl}}$ and $\boldsymbol{S_w}$ for the coastal GOM station.

Optics EXPRESS

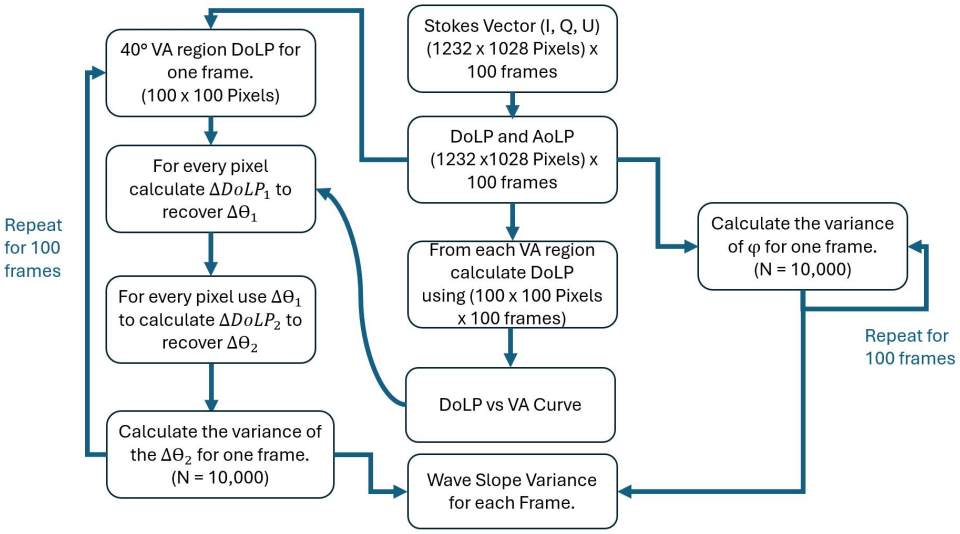

Fig. 9. Diagram for retrieval of the angle $\Delta\theta_2$ related to the skylight reflectance from the wave facet in the PSSm technique.

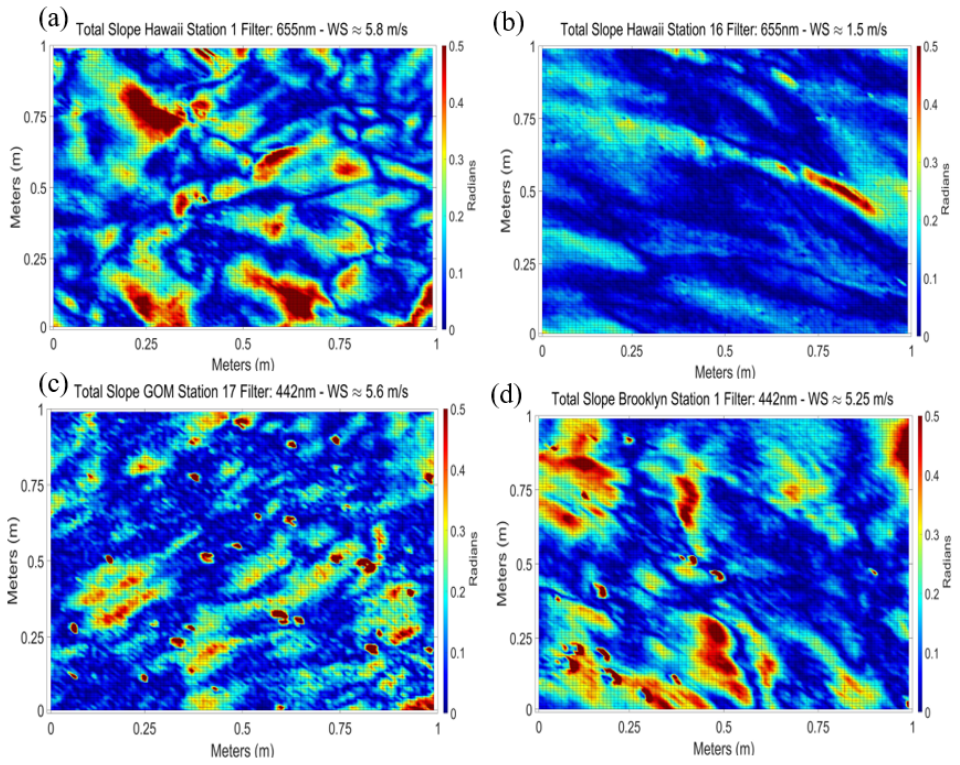

Fig. 10. Instantaneous slopes derived from the pair of angles ($\Delta\theta_2$, φ) from camera observations for the a) and b) Hawaii cruise (WS = 5.8 and 1.5 m/s), c) for GOM and d) Brooklyn Pier stations.

The φ components of the wave slopes determined through the AoLP were taken directly as measured from the camera as there was no mechanism to separate effects from the water and

Optics EXPRESS

reflected sky. The total maximum slopes, which could be measured were about 20-25°, which should be satisfactory to characterize slopes for at least WS < 10 m/s observed in the field. For clarity, the algorithm described above is also explained in the diagram shown in Fig. 9.

The instantaneous slopes retrieved from the camera observations are shown in Fig. 10 for three water areas and two wind speeds (WS = 5.8 and 1.5 m/s) for the Hawaii cruise. The slopes are shown for the central part of the camera FOV with 100×100 pixels and the distance in the azimuth direction is about 1 m and about 1 m in the viewing direction. The slope structure is similar for all three cruises where wind speed was about 5.5 m/s, and the scales are larger at the Hawaii station when WS = 1.5 m/s. The slopes' structure is also consistent with similar observations of Laxague et al, 2015 [38] (Fig. 5(a)) where the resolution of the camera was about times greater than ours.

The slope distributions shown in Fig. 11 follow a Gaussian fit and are represented for the VA = 40° for a total of 100 frames. Each distribution pair of ($\Delta\theta_2$, φ) contains a million wave slope data points acquired from the video in the central part of the FOV 100×100 pixels over 10 seconds. The φ component fits well the Gaussian distribution, $\Delta\theta_2$ component fit is less accurate, which could be due to the established procedure of $\Delta\theta_2$ calculation in conditions of some glint effects and breaking waves introducing additional data noise.

Examples of slopes processed from 100 frames with this approach for four filters and one example station from each water area of study are shown in Fig. 12. The instantaneous wave slope variance is computed for each frame (for 100×100 pixels) and the average from 100 frames is given in the legend representing the wave slope variance for that station.

CM wave slope statistics [1] assume zero mean and on the average flat-water surface where σ is the wave slope, $\sigma = 0$, and the variance of the slopes in Eq. (12a) is equal to the mean of the squared slope (*mss*).

Furthermore, two directional variances are added as in the case of wave slopes in Eq. (12b) where axes are in the along-wind and crosswind directions. Our polarimetric measurements observations were at 90° azimuth angle and thus were not aligned with the wind direction, so comparisons with CM are made based on Eq. (12c) without considering wind direction.

$$mss = var(\sigma) = \sum_1^N \frac{\sigma^2 - \sigma}{N} = \sum_1^N \frac{\sigma^2}{N} = \langle \sigma^2 \rangle \tag{12a}$$

$$mss = \langle \sigma_t^2 \rangle = \langle \sigma_a^2 \rangle + \langle \sigma_c^2 \rangle \tag{12b}$$

$$\sigma_t^2 = \sigma_a^2 + \sigma_c^2 = 0.003 + 5.12E^{-3}WS \ \pm 0.004 \tag{12c}$$

In Fig. 12 time series of wave slope variances are compared with CM expressions Eq. (12c) with the data computed for 100 frames and averaged over 100×100 pixels for each frame. At the same station, slope variances are similar for all measured wavelengths with some exceptions, where they have greater frame-by-frame variability. Wave slope variances are close to CM predicted values after averaging for all 100 frames but typically with larger standard deviations than in Eq. (12c), which at least partially can be due to arbitrary conditions of glint and breaking waves and modulation wave slopes by longer waves. DoLP curves from different color filters, in general, follow the logic described above being consistent with spectral changes of the water absorption in the corresponding water area DoLP vs. VA dependence is like the DoLP curve in Fig. (6(b)) but with significantly different DoLP values at different colors and in different waters. The PSSm technique is concerned not with DoLP values but with the DoLP changes due to the reflected sky $\Delta DoLP_2$, which define deviations of the DoLP in both directions from the viewing angle of 40°.

The most reliable results were achieved with the DoLP vs. VA curves, which correspond to higher DoLP values and thus with the highest sensitivity of the DoLP to VA and closest to the Fresnel curve. In the open ocean, those were the curves from the red 655 nm filter and for the

Optics EXPRESS

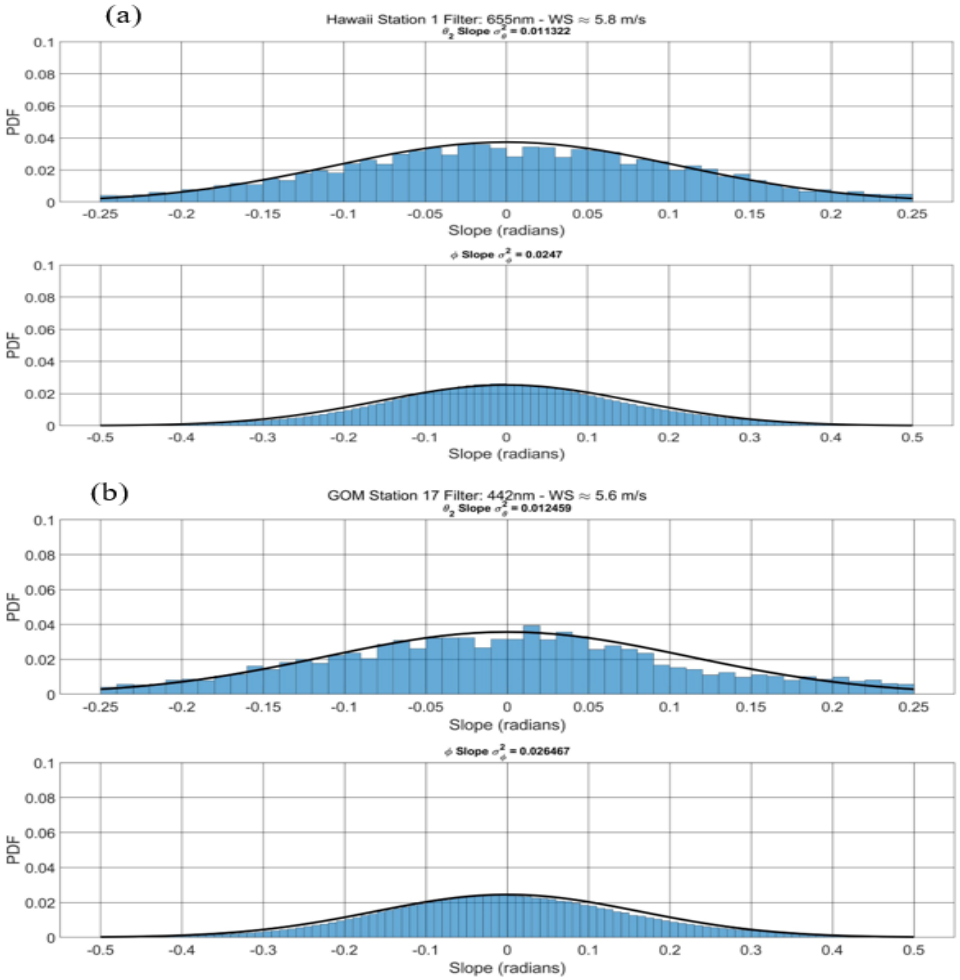

Fig. 11. Distribution of slopes derived from the pair of angles ($\Delta\theta_2$, φ) from camera observations a) for the Hawaii cruise (WS = 5.8 m/s) and b) for GOM (WS = 5.6 m/s). The respective Gaussian curve (black) is provided for the given variance of the distribution.

coastal waters from the blue 443 nm filter with some mixture for the Newport cruise, where waters were semi-coastal. This is consistent with the contribution of the L_s to L_t shown in Fig. 3 and 4. The described technique to determine $\Delta DoLP_{sky}$, angular deviations $\Delta\theta_1$ and $\Delta\theta_2$ and to select DoLP vs. VA from the specific color filter was called the modified PSS technique or PSSm with results averaged over 100×100 pixels and 100 frames shown in Fig. 13.

The data from all color filters is shown in Fig. 14 and the combined data from Fig. 13 is shown in Fig. 15 demonstrating the efficiency of the PSSm technique and its applicability for various water conditions in terms of the separation of the sky and water components and selection of the specific filter. The data in Fig. 15 is also very consistent with CM variances for the wind speed range from 0 to almost 10 m/s confirming that CM relationships are appropriate to use in various water conditions and in coastal and even near shore water areas.

Optics EXPRESS

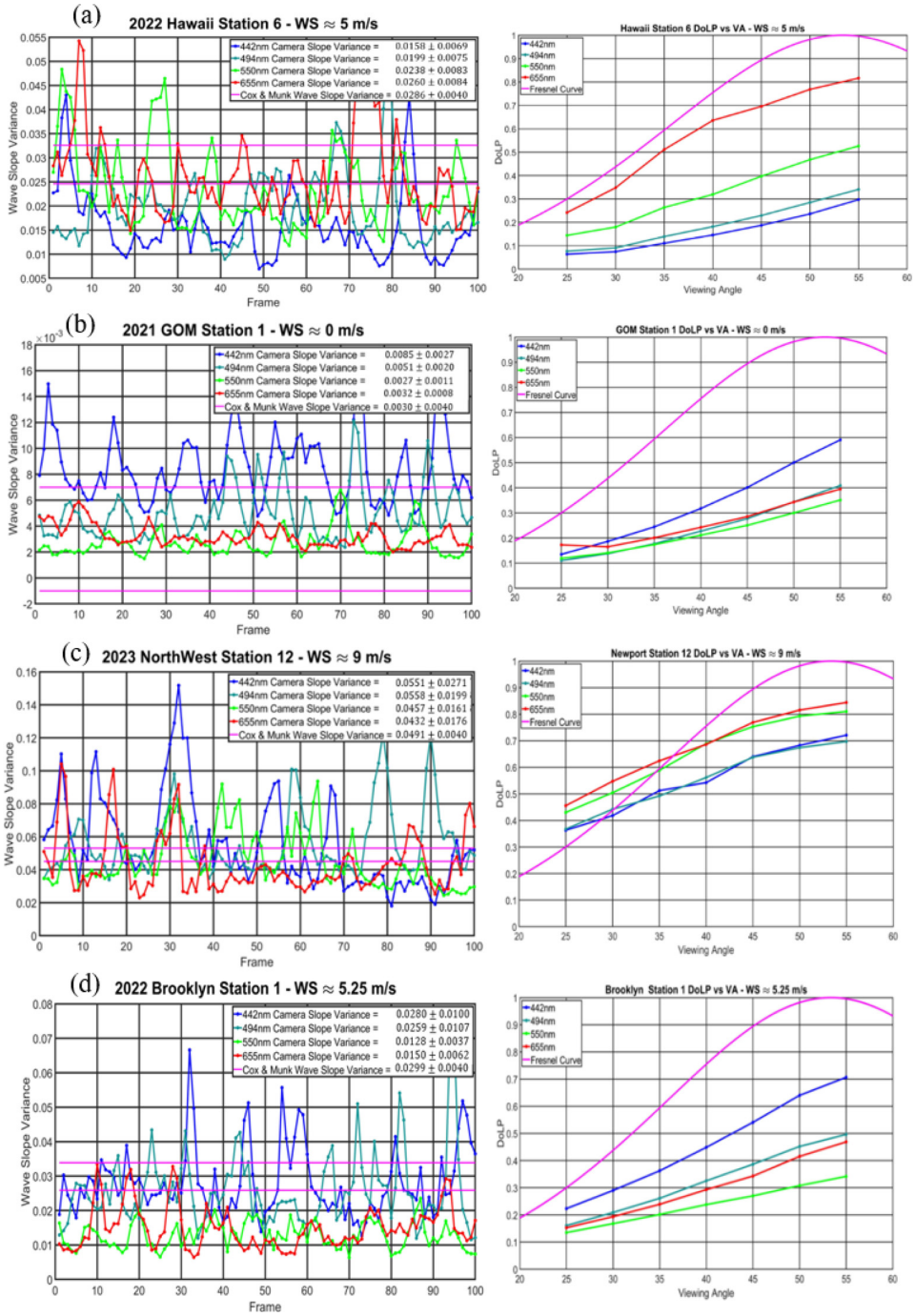

Fig. 12. Wave slope variances (left) and DoLP vs VA curves (right): a) Hawaii Station 6; b) GOM Station 1; c) Newport Station 12; d) Brooklyn Station 1.

Optics EXPRESS

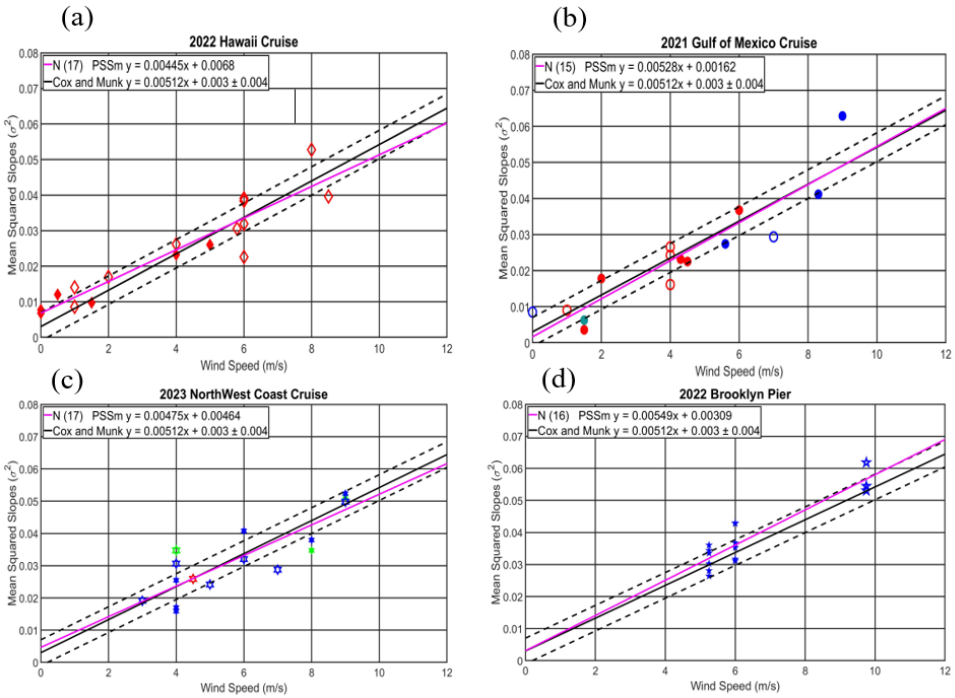

Fig. 13. The camera recorded mean square slopes vs. wind speed for a) 2022, b) 2021, c) 2023 VIIRS Cal/Val Cruises and d) Brooklyn Pier. The colors represent which color filter 442 nm (blue), 494 nm (cyan), 550 nm (green), or 655 nm (red) was selected using DoLP vs. VA curve criteria. The corresponding Sun zenith angle is shown by filled markers (around noon time) zenith with the angle at 25 to 35° and empty markers (morning and evening) with the angle greater than 35°.

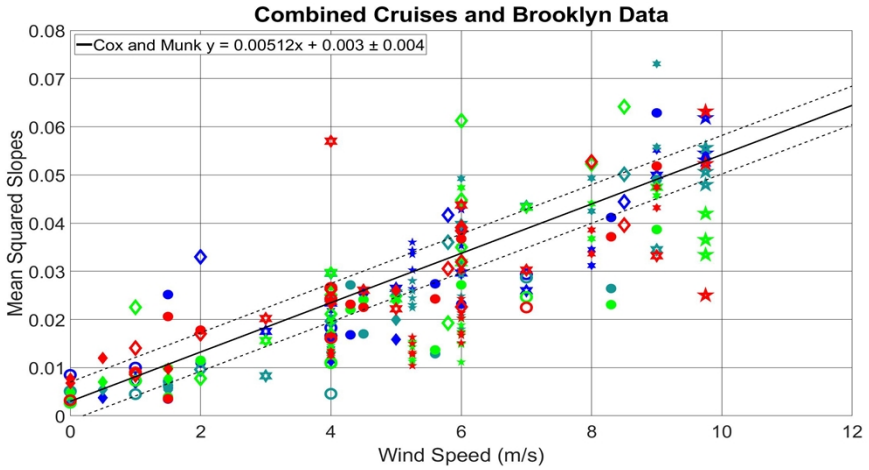

Fig. 14. Combined all mean squared slope data from Hawaii (diamond), Gulf of Mexico (circle), Brooklyn (star), and Newport (hexagram) for color filters 442 nm (blue), 494 nm (cyan), 550 nm (green), and 655 nm (red).

Optics EXPRESS

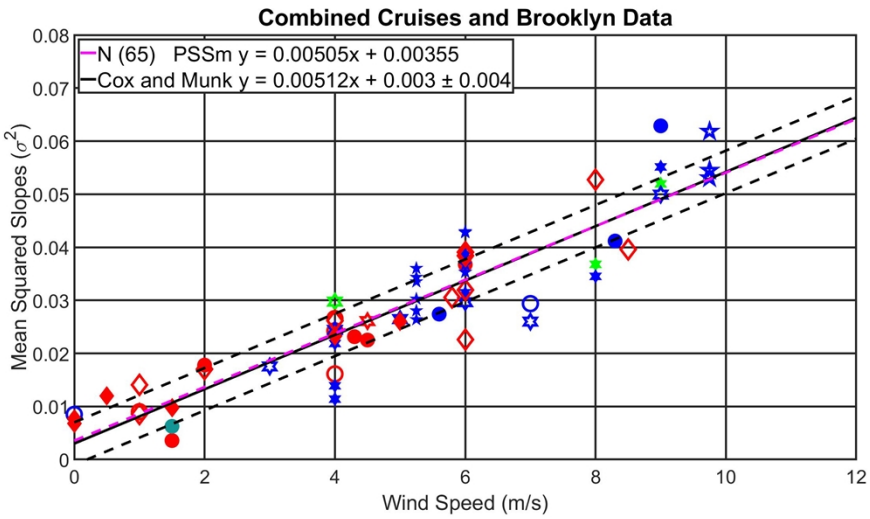

Fig. 15. Combined highest DoLP vs. VA mean squared slope data from Hawaii (blue), Gulf of Mexico (cyan), Brooklyn (green), Newport (red), and best-fit line using those data points (magenta).

3.3. *Wave slope variances and wave spectra*

To understand the ocean surface interactions and wave structures, the omnidirectional wave slope spectra $P(k)$ and wave elevation spectra $S(k)$ of the ocean surface are considered, where $k = 2\pi/\lambda$ is the wavenumber in radians/m and λ is the wavelength in m. These spectra give insight in the transformation from gravitational to capillary wave type as a function of the wavenumber [38]. One of the basic models is the Pierson-Moskowitz model [46], which describes gravity waves at a fully developed sea at a steady-state wave field assuming steady wind over infinite time at an infinite area. The Pierson-Moskowitz model is used to analyze mostly long waves with low wavenumbers below resolved in our experiments. Another model of Elfouhaily et al. [47] considers gravity-capillary wave spectrum at different sea states (Ω) from young (Ω=5) to fully developed (Ω=0.84). In the fully developed sea, this model is very close to Pierson-Moskowitz model below $k = 10$ rad/m region, and in addition, the Elfouhaily et al. model distinguishes gravitational waves below $k = \sqrt{\rho g/\tau} = 370\ rad/m$ and mostly capillary waves above this number, where ρ is the density of the sea, g is the gravitational acceleration, and τ is the surface tension. The relationship between the omnidirectional wave slope spectrum and the wave elevation spectrum is given in Eq. (13a) [17]. With $P(k)$ and $S(k)$ spectra the integration over the total spatial wavenumber spectrum will result in the wave slope variance σ^2 and the wave elevation variance z^2 respectively, as shown in Eq. (13b) and Eq. (13c). Integration over a desired spatial wavenumber range can be performed to see the difference in the contribution of gravitational and capillary waves to the total wave slope variance and wave elevation variance. The integration of the $P(k)$ over the range of $k = 10^{-2}$ to $k = 10^4$ is sufficient to represent the whole spectrum for both Pierson-Moskowitz and Elfouhaily et al. models and can be compared with Cox and Munk variance statistics.

$$P(k) = k^2\, S(k) \tag{13a}$$

$$\sigma^2 = \int_0^\infty P(k)d\mathrm{k} \tag{13b}$$

$$z^2 = \int_0^\infty S(k)dk \tag{13c}$$

Optics EXPRESS

Cruises and Brooklyn pier measurements were carried out at an altitude of 10 m and the VA = 40° camera central region sees a physical water surface of about L = 1 m by 1 m. The maximum wavenumber recovered by the camera measurement that satisfies the Nyquist criterion is $k_{max} = \pi/\Lambda$ where Λ is the camera's spatial resolution in meters per pixel $\Lambda = L/N$, which corresponds to $k_{x\,max} = k_{y\,max} = 314\ rad/m$. The fundamental wavenumber of the camera is $k_x = k_y = \frac{2\pi}{L} = 6.28\ rad/m$. Using $k = \sqrt{k_x^2 + k_y^2}$ the maximal omnidirectional spatial wavenumber is $k_{max} = 445\ rad/m$ and the minimal number is $k_{min} \approx 9\ rad/m$, which defines the range of the wavenumbers captured by the camera as 6-314 rad/m in one direction and 9–445 rad/m for the total, which were used further in the integration. The camera area in the VA = 40° is adjusted to a square region of 99 × 99 pixels, which results in a drop of the spectra starting near k = 314 rad/m due to inadequate sampling on the edges of the camera. Here x and y directions correspond to the directions, in which θ_2 and φ were determined.

The use of the PSSm technique allows to compare the theoretical models for $P(k)$ and $S(k)$ with the wave slopes variance data measured by the camera data similar to Laxague et al. [38]. The two slope fields σ_x and σ_y correspond to the $\Delta\theta_2$ and φ recovered by the camera and their Fourier transforms are given by σ_{XFT} and σ_{YFT} respectively Eq. (14a, 14b). The σ_{XFT} and σ_{YFT} are then used to find the wave slope spectra P_x and P_y using Eq. (14c) where N is the number of pixels. The P_x and P_y are then added and transformed into the omnidirectional spectrum $P(k)$ as shown in Eq. (14d, 14e, 14f).

$$\sigma_{XFT} = \int_{-\infty}^{\infty}\int_{-\infty}^{\infty} e^{j(xk_x+yk_y)}\sigma_x(x,y)dxdy \tag{14a}$$

$$\sigma_{YFT} = \int_{-\infty}^{\infty}\int_{-\infty}^{\infty} e^{j(xk_x+yk_y)}\sigma_y(x,y)dxdy \tag{14b}$$

$$P_x(k_x,k_y) = \frac{|\sigma_{XFT}|^2}{Nk_{x\,max}\,k_{y\,max}}\ ,\ P_y(k_x,k_y) = \frac{|\sigma_{YFT}|^2}{Nk_{x\,max}\,k_{y\,max}} \tag{14c}$$

$$P(k_x,k_y) = P_x + P_y\ ,\ P(k,\alpha) = kP(k_x,k_y) \tag{14d}$$

$$k = \sqrt{k_x^2+k_y^2},\ \alpha = \tan\left(\frac{k_y}{k_x}\right) \tag{14e}$$

$$P(k) = \sum_{\alpha=0}^{\alpha=2\pi} P(k,\alpha) \tag{14f}$$

The $S(k)$ and $P(k)$ spectra for one of the stations are shown in Fig. 16 and compared with the theoretical model of Elfouhaily et al. for the same location. The camera spectra $S(k)$ and $P(k)$ spectra are shown from an average of 100 frames recorded over 10 s with major σ outliers omitted, examples of which were visible in Fig. 12. The integration of the camera's total $P(k)$ spectra is performed and compared with Elfouhaily et al. wave slope variance (σ^2). The integration of $S(k)$ is performed in the same manner to derive wave elevation variance (z^2) which is used to calculate the significant wave height ($H_{1/3} = 4\sqrt{z^2}$) defined as the height from trough to crest distance of the highest one-third of the waves. Similar spectra from measurements at different geographical locations with different sea states (Ω) are presented in Fig. 17, where only spectra from filters used in the PSSm technique are shown.

The *mss* are verified using Eq. (13b) where the integration of the camera's P(k) spectrum results in the original *mss* values. All spectra, especially $P(k)$, are noisy because of the short time of acquisition (10 s) for each filter with increased noise after 100-200 rad/m closer to the k_{max} of the camera measurements; all spectra follow the features of Elfouhaily et al. in this spectral region, specifically an increase after ~100 rad/m. σ^2 calculated for the camera measurements from the 655 nm for Hawaai and 442 nm filter for GoM and Brooklyn are very close to the σ^2 from Elfouhaily et al. model, while there are mostly larger differences for other filters. Calculations of the significant wave height by the integration of the $S(k)$ spectra appeared to be more sensitive to

Optics EXPRESS

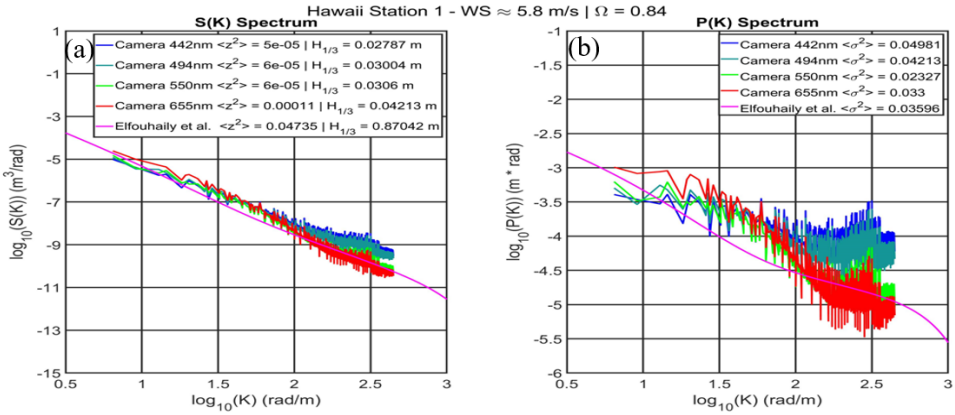

Fig. 16. Omnidirectional a) $S(k)$ and b) $P(k)$ spectra derived from the camera with comparison to Elfouhaily et al. model for the Hawaii station with data from all filters. The integrated spectra of $S(k)$ and $P(k)$ over the full wavenumber range of the camera are compared with the integration of Elfouhaily et al. models over $k = 10^{-2}$ to 10^{4} rad/m. For this station 655 nm filter (red) was used in the PSSm technique.

the small wavenumber interval of the camera measurements with $H_{1/3}$ much smaller than from Elfouhaily et al. model and differences increasing with the wind speed. Results are consistent with the literature [16,17] stating that the $S(k)$ spectra are less dependent on sampling frequency than the $P(k)$ spectra which have more oscillations.

Thus, the differences between the measurements and the model are most likely due to limits of the spatial frequencies which can be resolved by the camera. This leaves out some longer and shorter waves, which contribute power to the spectra visible on the graphs. The effect is smaller at lower wind speeds as demonstrated for Hawaii station 16 in Fig. 17. It should be also reminded that all measurements were carried out in sunny sky conditions, so the presence of the sun glint and breaking waves, especially at high wind speeds could contribute to the differences between spectra from the model and the measurements.

The results of the PSSm technique application for wave slope spectra retrievals show close correlations with the theoretical models and thus prove the feasibility of the technique. For a better understanding of the spatial spectra behavior, a better resolution of the camera would be needed to capture smaller capillary waves and to verify the spectra at higher spatial frequencies. A series of measurements with the polarimetric camera and PSSm technique in various conditions can help in understanding the air-ocean interactions at the surface and the dynamics of these waves.

Optics EXPRESS

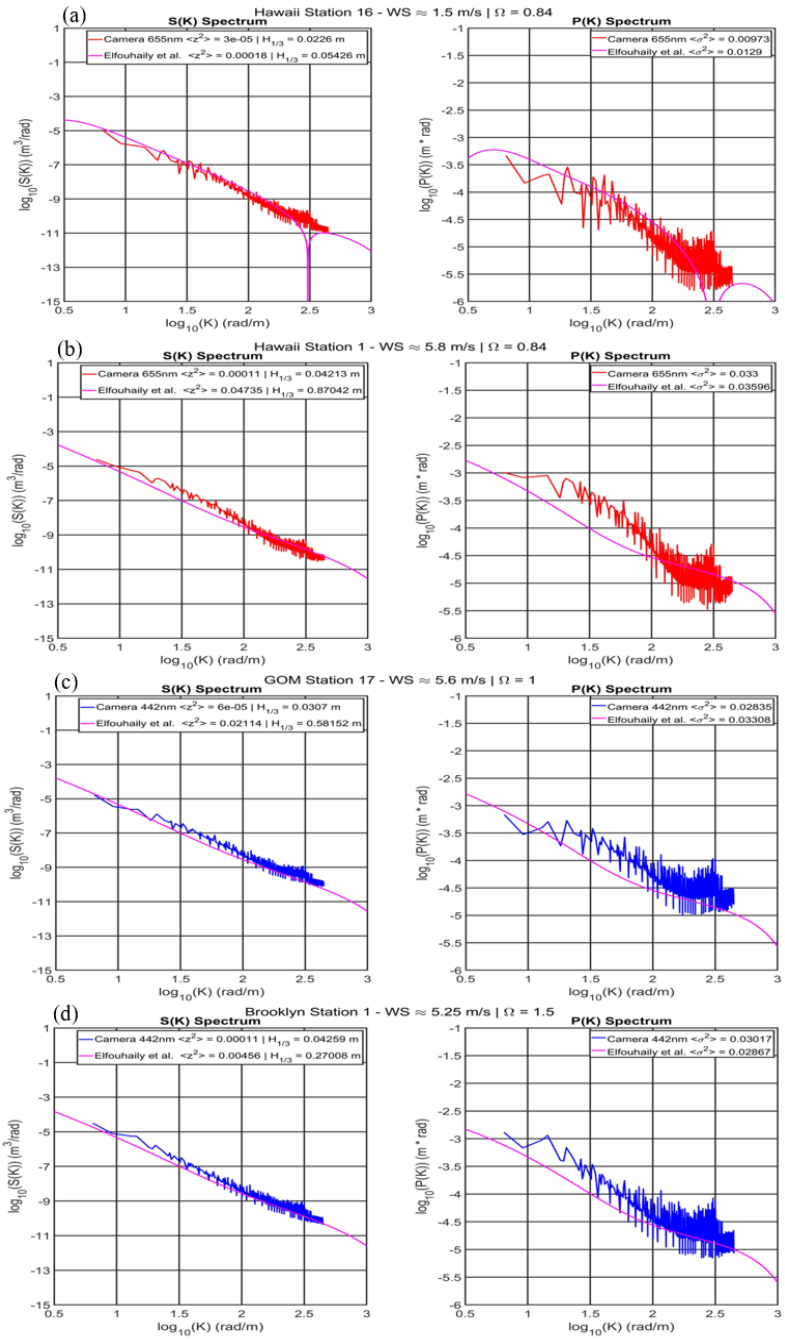

Fig. 17. Omnidirectional $S(k)$ (left) and $P(k)$ (right) spectra derived from the camera with comparison to the Elfouhaily et al. model at different sea states (Ω) for (a-b) Hawaii, c) Gulf of Mexico and d) Brooklyn. The integrated spectra of $S(k)$ and $P(k)$ over the full wavenumber range of the camera are compared with the integration of Elfouhaily et al. models over $k = 10^{-2}$ to 10^{4} rad/m. For the Hawaii stations, 655 nm filter (red) was used in the PSSm technique, 442 nm filter (blue) for GOM and Brooklyn.

Optics EXPRESS

4. Conclusions

The imaging system, containing the polarimetric imaging camera was successfully used for measurements of the Stokes vector components from the ships in the Gulf of Mexico, Hawaii, and Newport, OR VIIRS validation cruises and from the pier in Brooklyn, NY, thus covering various water conditions from open ocean to coastal waters in a broad range of wind speeds. Modified polarization slope sensing technique PSSm, which uses measured DoLP vs VA curves at different wavelengths instead of modeled curves from Fresnel equations with a special separation of the upwelling radiance and reflected sky components thus improving the original PSS technique [37], was applied to determine wave slope variances in these various water and wind conditions and mostly clear skies. It is shown that retrieved variances in most cases are in the range calculated by the Cox-Munk relationships with standard deviations included for the open ocean, coastal waters, and even near-shore areas. A reasonable matchup is observed between the Elfouhaily et al. model and the camera-measured wave slope $P(k)$ and wave elevation $S(k)$ spectra with some differences observed at high wind speeds due to the limitation of the camera's spatial resolution. These results are important in terms of the estimation of the effects of the skylight reflectance from the water surface in various water areas with different sea states since this reflectance is used in the calculation of the water leaving radiance and remote sensing reflectance in above water measurements and in atmospheric correction models.

Funding. National Aeronautics and Space Administration (80NSSC21K0562); National Oceanic and Atmospheric Administration (CESSRST Center, JPSS Cal/Val program, JPSS PGRR program); Office of Naval Research.

Acknowledgments. The authors are grateful to four reviewers, whose comments led to the significant improvement of the manuscript. We also thank Dr. Nathan Laxague from the University of New Hampshire for important comments and suggestions.

Disclosures. The authors declare no conflicts of interest.

Data availability. Data underlying the results presented in this paper are available upon request from the corresponding author.

References

1. C. Cox and W. Munk, "Measurement of the roughness of the sea surface from photographs of the sun's glitter," J. Opt. Soc. Am. **44**(11), 838–850 (1954).
2. H. R. Gordon and M. Wang, "Surface-roughness considerations for atmospheric correction of ocean color sensors. I: The Rayleigh-scattering component," Appl. Opt. **31**(21), 4247–4260 (1992).
3. H. R. Gordon and M. Wang, "Retrieval of water-leaving radiance and aerosol optical thickness over the oceans with SeaWiFS: a preliminary algorithm," Appl. Opt. **33**(3), 443–452 (1994).
4. A. K. Fung and K. S. Chen, *Microwave Scattering and Emission Models for Users* (Artech House, 2010), pp. 430.
5. C. Goyens and K. Ruddick, "Improving the standard protocol for above-water reflectance measurements: 1. Estimating effective wind speed from angular variation of sunglint," Appl. Opt. **62**(10), 2442–2455 (2023).
6. V. Capelle and J.-M. Hartmann, "Use of hyperspectral sounders to retrieve daytime sea-surface temperature from mid-infrared radiances: Application to IASI," Remote Sens. Environ. **280**, 113171 (2022).
7. A. M. Sayer, G. E. Thomas, and R. G. Grainger, "A sea surface reflectance model for (A)ATSR, and application to aerosol retrievals," Atmos. Meas. Tech. **3**(4), 813–838 (2010).
8. F. M. Bréon and N. Henriot, "Spaceborne observations of ocean glint reflectance and modeling of wave slope distributions," J. Geophys. Res. **111**(C6), C06005 (2006).
9. V. Ross and D. Dion, "Sea surface slope statistics derived from Sun glint radiance measurements and their apparent dependence on sensor elevation," J. Geophys. Res. **112**(C9), C09015 (2007).
10. B. Hughes, H. Grant, and R. Chappell, "A fast response surface-wave slope meter and measured wind-wave moments," Deep-Sea Res. **24**(12), 1211–1223 (1977).
11. S. Haimbach and J. Wu, "Field trials of an optical scanner for studying sea-surface fine structures," IEEE J. Oceanic Eng. **10**(4), 451–453 (1985).
12. P. A. Hwang and O. H. Shemdin, "The dependence of sea surface slope on atmospheric stability and swell conditions," J. Geophys. Res. **93**(C11), 13903–13912 (1988).
13. J. A. Shaw and J. H. Churnside, "Scanning-laser glint measurements of sea-surface slope statistics," Appl. Opt. **36**(18), 4202–4213 (1997).

Optics EXPRESS

14. L. Lenain, N. M. Statom, and W. K. Melville, "Airborne Measurements of Surface Wind and Slope Statistics over the Ocean," Bull. Am. Meteorol. Soc. **49**(11), 2799–2814 (2019).
15. C. A. Guérin, V. Capelle, and J. M. Hartmann, "Revisiting the Cox and Munk wave-slope statistics using IASI observations of the sea surface," Remote Sens. Environ. **288**, 113508 (2023).
16. C. D. Mobley, *Ocean Optics Web Book*, (http://www.oceanopticsbook.info/, 2020).
17. C. D. Mobley, *Modeling Sea Surface A Tutorial on Fourier Transform Techniques* (Sequoia Scientific, Inc., 2016), Chap. 2.
18. A. Gilerson, E. Herrera-Estrella, R. Foster, *et al.*, "Determining the Primary Sources of Uncertainty in Retrieval of Marine Remote Sensing Reflectance from Satellite Ocean Color Sensors," Front. Remote Sens. **3**, (2022).
19. A. Gilerson, E. Herrera Estrella, J. Agagliate, *et al.*, "Determining the primary sources of uncertainty in the retrieval of marine remote sensing reflectance from satellite ocean color sensors II. Sentinel 3 OLCI sensors," Front. Remote Sens. **4**, (2023).
20. C. D. Mobley, "Estimation of the remote-sensing reflectance from above-surface measurements," Appl. Opt. **38**(36), 7442–7455 (1999).
21. M. I. Mishchenko and L. D. Travis, "Satellite retrieval of aerosol properties over the ocean using polarization as well as intensity of reflected sunlight," J. Geophys. Res. **102**(D14), 16989–17013 (1997).
22. M. Gao, B. A. Franz, K. Knobelspiesse, *et al.*, "Efficient multiangle polarimetric inversion of aerosols and ocean color powered by a deep neural network forward model," Atmos. Meas. Tech. **14**(6), 4083–4110 (2021).
23. M. Gao, K. Knobelspiesse, B. A. Franz, *et al.*, "Adaptive Data Screening for Multi-Angle Polarimetric Aerosol and Ocean Color Remote Sensing Accelerated by Deep Learning," Front. Remote Sens. **2**, (2021).
24. M. Chami, R. Santer, and E. Dilligeard, "Radiative transfer model for the computation of radiance and polarization in an ocean-atmosphere system: polarization properties of suspended matter for remote sensing," Appl. Opt. **40**(15), 2398 (2001).
25. H. Loisel, L. Duforet, D. Dessailly, *et al.*, "Investigation of the variations in the water leaving polarized reflectance from the POLDER satellite data over two biogeochemical contrasted oceanic areas," Opt. Express **16**(17), 12905–12918 (2008).
26. A. Tonizzo, A. Gilerson, T. Harmel, *et al.*, "Estimating particle composition and size distribution from polarized water-leaving radiance," Appl. Opt. **50**(25), 5047–5058 (2011).
27. A. Ibrahim, A. Gilerson, T. Harmel, *et al.*, "The relationship between upwelling underwater polarization and attenuation/absorption ratio," Opt. Express **20**(23), 25662–25680 (2012).
28. A. Ibrahim, A. Gilerson, J. Chowdhary, *et al.*, "Retrieval of macro-and micro-physical properties of oceanic hydrosols from polarimetric observations," Remote Sens. Environ. **186**, 548–566 (2016).
29. J. Lotsberg and J. Stamnes, "Impact of particulate oceanic composition on the radiance and polarization of underwater and backscattered light," Opt. Express **18**(10), 10432–10445 (2010).
30. X. Zhang, S. He, A. Shabani, *et al.*, "Spectral sea surface reflectance of skylight," Opt. Express **25**(4), A1–A13 (2017).
31. A. Gilerson, C. Carrizo, R. Foster, *et al.*, "Variability of the reflectance coefficient of skylight from the ocean surface and its implications to Ocean Color," Opt. Express **26**(8), 9615–9633 (2018).
32. C. Jamet, A. Ibrahim, Z. Ahmad, *et al.*, "Going Beyond Standard Ocean Color Observations: Lidar and Polarimetry," Front. Mar. Sci. (6),(2019).
33. C. D. Mobley, "Polarized reflectance and transmittance properties of windblown sea surfaces," Appl. Opt. **54**(15), 4828–4849 (2015).
34. P.J. Werdell, M.J. Behrenfeld, P.S. Bontempi, *et al.*, "The Plankton, Aerosol, Cloud, ocean Ecosystem (PACE) mission: Status, science, advances," Bull. Am. Meteorol. Soc. **100**(9), 1775–1794 (2019).
35. A. Gilerson, C. Carrizo, A. Ibrahim, *et al.*, "Hyperspectral polarimetric imaging of the water surface and retrieval of water optical parameters from multi-angular polarimetric data," Appl. Opt. **59**(10), C8–C20 (2020).
36. J. Agagliate, R. Foster, A. Ibrahim, *et al.*, "A neural network approach to the estimation of in-water attenuation to absorption ratios from PACE mission measurements," Front. Remote Sens. (4), (2023).
37. C. J. Zappa, M. L. Banner, H. Schultz, *et al.*, "Retrieval of short ocean wave slope using polarimetric imaging," Meas. Sci. Technol. **19**(5), 055503 (2008).
38. N. J. Laxague, B. K. Haus, D. Bogucki, *et al.*, "Spectral characterization of fine-scale wind waves using shipboard optical polarimetry," J. Geophys. Res. Oceans. **120**(4), 3140–3156 (2015).
39. J. L. Pezzaniti, D. Chenault, M. Roche, *et al.*, "Wave Slope Measurement Using Imaging Polarimetry," Proc. SPIE 7317, (2007).
40. J. Agagliate, M. Malinowski, E. Herrera, *et al.*, "Polarimetric imaging of the ocean surface for satellite-based ocean color applications," Proc. SPIE **12112**, 18 (2022).
41. M. Malinowski, A. Gilerson, E. Herrera, *et al.*, "Polarimetric imaging of the ocean surface for the study of ocean surface roughness and wave slopes statistics," Proc. SPIE **12543**, 23 (2023).
42. H. R. Gordon, T. Du, and T. Zhang, "Atmospheric correction of ocean color sensors: analysis of the effects of residual instrument polarization sensitivity," Appl. Opt. **36**(27), 6938–6948 (1997).
43. N. A. Umov, "Chromatische depolarisation durch lichtzerstreuung," Physikalische Zeitschrift **6**, 674–676 (1905).
44. H. H. Tynes, G. W. Kattawar, E. P. Zege, *et al.*, "Monte Carlo and multicomponent approximation methods for vector radiative transfer by use of effective mueller matrix calculations," Appl. Opt. **40**(3), 400–412 (2001).

Optics EXPRESS

45. R. Foster and A. Gilerson, "Polarized Transfer Functions of the Ocean Surface for Above-Surface Determination of Vector Submarine Light Field," Appl. Opt. **55**(33), 9476–9494 (2016).
46. W. J. Pierson and L. Moskowitz, "A proposed spectral form for fully developed wind seas based on the similarity theory of S. A. Kitaigorodskii," J. Geophys. Res. **69**(24), 5181–5190 (1964).
47. T. Elfouhaily, B. Chapron, K. Katsaros, *et al.*, "A unified directional spectrum for long and short wind-driven waves," J. Geophys. Res. **102**(C7), 15781–15796 (1997).